PAPER

Check for updates

CO₂ reduction by dielectric barrier discharge plasma in collaboration with $Cu_{2-x}Se/AlO(OH)$ catalyst

Yi Chen,[a] Weilin Shi,[a] Claudia Li, [b] Kang Hui Lim, [b] Xueqian Wang, [ac] Langlang Wang,[ac] Ping Ning,[ac] Yixing Ma*[abc] and Sibudjing Kawi [b] *[b]

Global warming, driven by rising levels of CO₂ in the atmosphere, is an environmental predicament confronted by humanity. Plasma catalytic decomposition of carbon dioxide into carbon monoxide is a practical approach to mitigate this challenge, which can be a crucial step in carbon recycling. Metal selenides are promising candidates owing to their abundant reserves and outstanding electron transfer properties, making them highly active in chemical reactions. In this study, the morphology of AlO(OH) and the dispersion of $Cu_{2-x}Se$ were optimized by hydrothermal synthesis temperature. Specifically, the $Cu_{2-x}Se$-Al-180 catalyst, prepared at a hydrothermal temperature of 180 °C, formed AlO(OH) with good crystallinity and a nanoscale thin-sheet structure, with $Cu_{2-x}Se$ uniformly distributed on the AlO(OH) support. The reaction of CO₂ decomposition to CO production by integrating $Cu_{2-x}Se$-Al-180 with dielectric barrier discharge (DBD) plasma led to a CO₂ conversion of up to 28.07% at a specific input energy (SIE) of 58.07 kJ L⁻¹. The excellent CO₂ adsorption properties of AlO(OH) and Cu₂Se reduce the activation energy barrier of the reaction, and Cu₂Se further promotes the excited activation of CO₂ in the plasma. These findings offer valuable insights for the development and design of catalysts in the field of plasma catalysis and highlight the potential of CuSe-based materials in CO₂ reduction technologies.

1. Introduction

In recent years, the harmful effects of the greenhouse effect on the environment have been a topic of discussion, as society has progressed and individuals have become more conscious of environmental protection.[1] To effectively mitigate CO₂ emissions, governments worldwide have actively pursued various policies and measures.[2]

In response to significant production of CO₂, current approaches mainly involve carbon capture, storage, and conversion.[3] The ultimate objective is to capture CO₂ in large quantities and efficiently convert it with minimal energy consumption, thereby addressing excessive CO₂ emissions and achieving carbon neutrality. Among these methods, direct decomposition of CO₂ into CO and O₂ is considered effective as the resulting CO can serve as a versatile chemical precursor in various industries.[4] However, the activation of CO₂ at ambient temperature and pressure poses challenges to the treatment process, hindering the subsequent reactions.[5] Consequently, the combination of light, electricity, and catalysts is commonly employed to overcome this obstacle and facilitate CO₂ decomposition.[6–8] Nevertheless, low utilization of light energy, catalyst deactivation, and electrode material loss present ongoing challenges in the CO₂ conversion process.[9,10] In contrast, dielectric barrier discharge (DBD) plasma demonstrates the ability to activate gases and promote the decomposition of CO₂ under ambient conditions.[11,12]

The use of DBD plasma alone is effective in activating gas, but the addition of a catalyst is often necessary to further reduce energy consumption and improve selectivity. Research efforts are currently focused on developing efficient and stable catalysts that can operate at low temperatures. Nanostructured metal compounds, such as oxides, sulfides,[13] and selenides, have been investigated for CO₂ reduction. Metal selenides have garnered significant attention due to their abundant reserves, low cost, and exceptional catalytic performance.[14,15] Selenium atoms in metal selenides exhibit robust electron transport capacity, allowing these compounds to possess catalytic properties similar to metals.[16] Furthermore, the light absorption properties, modifiable band structure, and adaptable local surface plasmon resonance features of metal selenides contribute to their significant potential in photoelectric catalysis.[17] Cuprous selenide, a semiconductor material, has been used in photocatalytic and electrocatalytic reduction of carbon

[a]Faculty of Environmental Science and Engineering, Kunming University of Science and Technology, Kunming, 650500, China

[b]Department of Chemical and Biomolecular Engineering, National University of Singapore, 117585, Singapore

[c]National-Regional Engineering Center for Recovery of Waste Gases from Metallurgical and Chemical Industries, Kunming University of Science and Technology, Kunming, 650500, China

This journal is © The Royal Society of Chemistry 2025

J. Mater. Chem. A, 2025, 13, 8445–8455 | 8445

dioxide.[18] However, its application in dielectric barrier discharge plasma requires further investigation. Studies have shown that cuprous selenide influences the quantity of active sites, CO_2 adsorption capacity, and kinetic characteristics of the catalyst.[19] In composite materials, cuprous selenide can act as a catalytic reaction center, enhancing the number of adsorption sites for reactions through synergistic interactions with the support material.[20] In addition, the choice of a suitable carrier is crucial. AlO(OH) has been identified as a carrier that can provide increased CO_2 adsorption sites owing to its large specific surface area and appropriate alkaline sites.[21,22] The structure of the catalyst support and the distribution of active elements significantly affect the overall efficiency of the catalyst.[23] Therefore, the process of catalyst preparation plays a crucial role in determining these aspects.

This work focuses on the single-step synthesis of $Cu_{2-x}Se$-AlO(OH) material using conventional hydrothermal treatment and investigates the influence of various hydrothermal temperatures on the crystallization of the catalyst carrier and the dispersion of active components. The resulting $Cu_{2-x}Se$-AlO(OH) catalyst possesses semiconductor properties and is utilized in conjunction with DBD plasma for the CO_2 decomposition reaction.

2. Experimental

2.1 Materials

Nano-alumina (γ-Al_2O_3, 99.9%) was purchased from Aladdin Reagent (China) Co., LTD. Copper nitrate ($Cu(NO_3)_2 \cdot 2.5H_2O$, AR), sodium hydroxide (NaOH, AR) and ethylenediamine tetraacetic acid ($C_{10}H_{16}N_2O_8$, AR), were obtained from Tianjin Fengboat Chemical Reagent Technology Co., LTD. Anhydrous sodium selenite (Na_2SeO_3, 99%) was supplied by Alfa Esha (China) Chemical Co., LTD. Hydrazine hydrate ($H_4N_2 \cdot H_2O$, AR, $\geq$80%) and hydrochloric acid (HCl, AR, 36–38%) were procured from Sichuan Xilong Science Co., LTD.

2.2 Catalyst preparation

The catalyst was synthesized by hydrothermal method, which is specified as follows: firstly, 28 mmol of NaOH was dissolved in 28 mL of deionized water. Then, 0.7 mmol of $Cu(NO_3)_2 \cdot 2.5H_2O$ and 6 mmol of EDTA were added successively to the solution. After ultrasonication for 30 min, 0.68 mmol of Na_2SeO_3 and 14 mL of hydrazine hydrate were added. Then the mixture was magnetically stirred for 10 min, and an appropriate amount of γ-Al_2O_3 was added during the stirring process. After stirring, the resulting mixture was transferred to a high-pressure Teflon-lined reactor with a capacity of 100 mL and treated for 6 h at 140 °C, 180 °C and 220 °C, respectively. After the hydrothermal treatment, the product was first treated with 1 M hydrochloric acid, then washed by deionized water and anhydrous ethanol for 3 times, and finally dried in a vacuum drying oven at 60 °C for 3 h to obtain $Cu_{2-x}Se$/AlO(OH). The catalyst was labeled as $Cu_{2-x}Se$-Al-y, where y represents the temperature of the hydrothermal treatment. The AlO(OH)-180 catalyst was produced by following the same steps as above without adding copper and

selenium sources under hydrothermal conditions at 180 °C. The material was simply ground before use.

2.3 Catalyst characterization

X-ray diffraction (XRD) was performed on a Brucker JV-DX X-ray diffractometer with operating voltages and currents of 40 kV and 40 mA, respectively. For the determination of pore and specific surface area of catalyst, the BET instrument AUTOSORB IQ was used to analyze pore volume and pore size through the adsorption and desorption curve data. X-ray photoelectron spectroscopy (XPS) tests were performed on a Thermo Scientific K-Alpha instrument with monochromatized Al Kα as a light source, an energy of 1486.6 eV, an operating voltage of 12 kV, and a filament power of 72 W. Tecnai G2 TF30 Philipps-FEI scanning electron microscope (SEM) and Tecnai G2 F20 S-TWIN high-resolution transmission electron microscope (HR-TEM) were used to analyze the morphology and structure of the catalyst. CO_2 temperature programmed desorption (CO_2-TPD) experiments were performed using a Micromeritics AutoChem II 2920 instrument to study the surface basicity of the materials. In addition, a plasma emission spectrometer (ULS2408, Avantes B.V.) was used during the experiment to capture the excited substances generated during the DBD plasma discharge to further explore the reaction mechanism. The capture range of the spectrum is 200–1000 nm.

In situ DRIFTS measurements were made using a Thermo Fisher Fourier Transform Infrared Spectrometer (iS50 FT-IR). It was first pretreated at 100 °C and 50 mL min^{-1} under N_2 atmosphere for 30 min, then cooled down to 25 °C, then N_2 purged for 10 min, and then the background spectra were collected. Then 20 mL min^{-1} pure CO_2 gas was introduced for 30 min. After adsorption saturation, CO_2 was turned off, and plasma discharge was turned on for 30 min, and the spectra were collected. The temperature of the reaction area was always kept at 25 °C during the plasma discharge to exclude the effect of temperature on the reaction. Each spectrum was recorded at an average of 64 scans with a resolution of 4 cm^{-1}.

2.4 Catalyst activity test

The device used in the experiment is shown in Fig. 1. The plasma power generator was provided by Nanjing Suman Plasma Technology Co., LTD. (Model: CTP-2000K), the power input voltage is 0–220 V, the output voltage is 0–40 kV, and the discharge frequency is maintained at 9 $\pm$ 0.1 kHz. The reactor that generates low temperature DBD plasma is a single dielectric coaxial tube structure. Quartz glass with an inner diameter of 22 mm, outer diameter of 26 mm, tube wall thickness of 2 mm and length of 300 mm is selected as the medium. A 400 mm long, 16 mm diameter solid rod of 304 stainless steel was used as the high-voltage electrode and a rubber plug was used to secure the high-voltage electrode to the center of the quartz tube. The grounding electrode is 200 mesh 304 stainless steel mesh, which is fixed to the outer wall of the quartz tube by Teflon insulation tape. For each experiment, quartz wool was used to hold the catalyst within a 15 mm long plasma discharge zone.
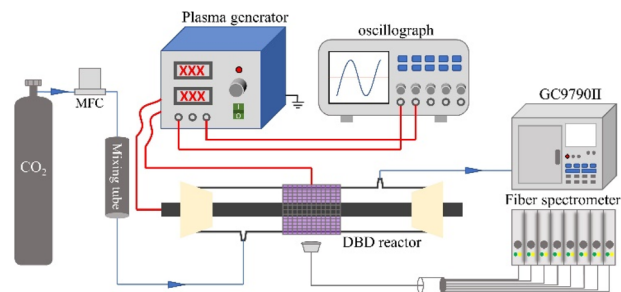
8446 | *J. Mater. Chem. A*, 2025, **13**, 8445–8455

This journal is © The Royal Society of Chemistry 2025

Fig. 1 Schematic diagram of experimental apparatus.

After the output voltage of the power supply is attenuated by 1000 times, it is monitored by the digital oscilloscope (model TDS 2024C, Tektronix) through the probe. A Lissajous curve is drawn according to the measurement data of the oscilloscope, and the plasma discharge power (P) and specific input energy (SIE) are further calculated to study the plasma discharge characteristics.

$$P(\text{kW}) = \frac{f \times C_m \times S}{1000} \quad (1)$$

$$\text{SIE}(\text{kJ L}^{-1}) = \frac{P}{[F]_{in}} \quad (2)$$

where f represents the output voltage frequency, kHz; C_m is the sampling capacitance inside the plasma power generator, which is 0.47 μF; S represents the average Lissajous graph area of a single period; $[F]_{in}$ represents the CO_2 inlet flow rate, L s^{-1}.

During the experimental procedure, CO_2 gas with a purity of 99.99% was introduced into the plasma reactor through a mass flow controller (MFC, D07-19B, Beijing Seven Star Electronics Co., LTD.) at a constant flow rate of 40 mL min^{-1}. Each time, samples were collected 30 min after the reaction had stabilized. The gas phase products were analyzed using an online gas chromatograph (Model GC-9790II) equipped with a column (Agilent J&W CarboPLOT P7), a thermal conductivity detector (TCD), and a hydrogen flame ionization detector (FID). An ozone analyzer (Model UV-100) was employed to determine the presence of ozone in the products with a sensitivity of 0.1 ppm. According to the test results, no ozone was produced during the experiment. In addition, the experiment did not detect carbon accumulation. This study mainly focused on the product CO, and the conversion rate measured by the CO_2 content at the inlet and outlet was within the experimental error range,[24] so the CO_2 conversion rate (X_{CO_2}) was calculated as follows:

$$X_{CO_2}(\%) = \frac{[CO_2]_{in} - [CO_2]_{out}}{[CO_2]_{in}} \times 100 \quad (3)$$

where $[CO_2]_{in}$ and $[CO_2]_{out}$ represent the import and export molar flows of CO_2, mol s^{-1}, respectively.

3. Results and discussion

3.1 Catalyst performance

DBD plasma was combined with catalysts prepared under various hydrothermal temperatures to facilitate CO_2
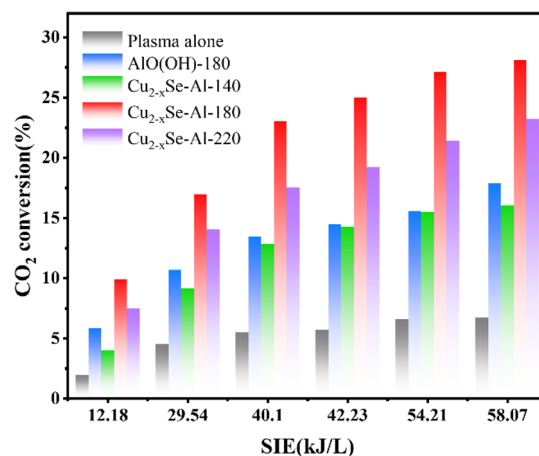

Fig. 2 Performance diagram of catalyst reaction in DBD plasma environment.

decomposition reactions. The efficacy of DBD plasma alone and DBD plasma in conjunction with AlO(OH)-180 catalyst was also evaluated, as shown in Fig. 2. Throughout the experiment, no additional carbon-based byproducts were detected, and complete conversion of CO_2 into carbon monoxide and oxygen occurred, and CO selectivity and carbon balance is about 100%.

Fig. 2 illustrates the relationship between SIE and voltage, showing a consistent increase in SIE as voltage rises. The CO_2 decomposition rates of standalone DBD plasma and DBD plasma combined with AlO(OH)-180, Cu_{2-x}Se-Al-140, Cu_{2-x}Se-Al-180, or Cu_{2-x}Se-Al-220 also demonstrate a steady ascent. This phenomenon can be attributed to the higher voltage levels, which enhance the electric field strength within the plasma discharge zone, thereby leading to increased excitation, ionization, and dissociation of the reaction gas.[25] DBD plasma possesses unique properties that allow for the decomposition of CO_2 when utilized independently, resulting in a CO_2 conversion rate of 6.72% at an SIE of 58.07 kJ L^{-1}. The coupling of DBD plasma with the catalysts significantly improved the CO_2 decomposition compared to plasma alone. Additionally, the combination of plasma with Cu_{2-x}Se-Al-140, Cu_{2-x}Se-Al-180, or Cu_{2-x}Se-Al-220 catalysts demonstrated distinct variations in CO_2 decomposition effectiveness. Among the three catalysts, Cu_{2-x}Se-Al-180 displayed the highest efficiency, with CO_2 conversion up to 28.07% at an SIE of 58.07 kJ L^{-1}. This was followed by Cu_{2-x}Se-Al-220, with a CO_2 conversion of 23.21% at the same SIE. The CO_2 conversion performance of Cu_{2-x}Se-Al-140 catalyst prepared at 140 °C was slightly lower than that of AlO(OH)-180 prepared at 180 °C, with a CO_2 conversion of 16.02% at an SIE of 58.07 kJ L^{-1}. These findings demonstrate the significant influence of hydrothermal temperature on catalyst activity. In a comprehensive comparison of energy and conversion efficiency, the Cu_{2-x}Se-Al-180 catalysts showed good performance compared with other reports.[26,27,45,51,56–61]

3.2 Morphology and structural analysis of catalysts

The catalyst was analyzed using XRD to determine its phase composition (Fig. 3). For comparative purposes, the AlO(OH)-

This journal is © The Royal Society of Chemistry 2025

J. Mater. Chem. A, 2025, **13**, 8445–8455 | **8447**

180 material, which was prepared under identical conditions to the Cu$_{2-x}$Se-Al-180 catalyst but without the addition of copper and selenium sources, was also subjected to XRD analysis for comparison. Moreover, the raw material, γ-Al$_2$O$_3$, was conducted too.

The XRD characterization results are displayed in Fig. 3a. The characteristic peaks of γ-Al$_2$O$_3$ are observed at 2θ values of 32.8°, 36.76°, 39.5°, 45.64°, 60.11°, and 66.98° (JCPDS 46-1131).[28] For the AlO(OH)-180 catalysts prepared without Cu and Se precursors, diffraction peaks appeared at 2θ values of 14.5°, 28.2°, 38.4°, 45.8°, 48.9°, 49.3°, 51.7°, 55.3°, 60.6°, 64.1°, 65.0°, 67.0°, 67.7° and 72.0°. These peaks correspond to the characteristic peaks of AlO(OH) (JCPDS 83-2384), indicating successful synthesis and modification of the γ-Al$_2$O$_3$ raw material to yield well-crystallized AlO(OH)-180 catalysts.[29] The AlO(OH) characteristic peaks were prominent in the Cu$_{2-x}$Se-Al-140, Cu$_{2-x}$Se-Al-180, and Cu$_{2-x}$Se-Al-220 catalysts prepared at 140 °C, 180 °C, and 220 °C hydrothermal conditions, respectively. The intensity of the AlO(OH) diffraction peaks increased with higher hydrothermal temperatures, suggesting improved AlO(OH) crystallinity in the Cu$_{2-x}$Se-Al-180 catalyst compared to the Cu$_{2-x}$Se-Al-140 catalyst. In addition, characteristic peaks of Cu$_2$Se were observed at 27.1°, 45.0°, 53.3° (JCPDS 88-2043). The introduction of Cu$_2$Se into the AlO(OH) carrier did not alter the crystal structure of AlO(OH), as indicated by the unchanged position of the AlO(OH) diffraction peak and decreased intensity. The effect has been reported in previous studies.[30] Additionally, the diffraction peaks of the Cu$_{2-x}$Se-Al-180 catalyst at 2θ values of 27.1° and 45.0° were broader and lower in intensity compared with those of Cu$_{2-x}$Se-Al-140 and Cu$_{2-x}$Se-Al-220 catalysts, suggesting superior dispersion of Cu$_2$Se in the Cu$_{2-x}$Se-Al-180 catalysts prepared under hydrothermal conditions at 180 °C.[31] However, the characteristic peaks of CuSe were not observed in XRD patterns, possibly due to the lower peak intensity of CuSe compared to Cu$_2$Se.[32,33]

Table 1 Structural characteristics of materials

Catalysts	S_{BET} (m^2 g^{-1})	Pore volume (cm^3 g^{-1})	Average pore size (nm)
γ-Al$_2$O$_3$	134.5	0.90	26.88
Cu$_{2-x}$Se-Al-140	120.8	0.77	23.12
Cu$_{2-x}$Se-Al-180	32.5	0.13	15.68
Cu$_{2-x}$Se-Al-220	33.1	0.19	22.37

The N$_2$ adsorption–desorption isothermal curves and pore size distribution curves of catalysts prepared at different hydrothermal temperatures are depicted in Fig. 3b. According to the IUPAC classification, all the isotherms in the figure are of type IV, suggesting that the catalyst possesses a mesoporous structure.[34] Nevertheless, notable distinctions can be observed in the hysteresis loops of the materials produced under varying hydrothermal conditions. Specifically, the Cu$_{2-x}$Se-Al-140 catalyst, synthesized at 140 °C, exhibits a H1 hysteresis similar to that of γ-Al$_2$O$_3$, indicating an ordered mesoporous structure in the material.[35] On the other hand, Cu$_{2-x}$Se-Al-180 and Cu$_{2-x}$Se-Al-220 materials, prepared at hydrothermal temperatures equal to or greater than 180 °C, display H3 type hysteresis loops, suggesting the material is composed of slit holes with flake particles.[36]

The detailed structural characteristics of the material are shown in Table 1. At a hydrothermal temperature of 140 °C, there is only a slight decrease in the specific surface area, pore volume, and pore diameter of the Cu$_{2-x}$Se-Al-140 catalyst compared to the raw material γ-Al$_2$O$_3$. The XRD pattern of Cu$_{2-x}$Se-Al-140 reveals the presence of poorly crystalline AlO(OH). This suggests that maybe only the outer layer of γ-Al$_2$O$_3$ transformed into AlO(OH) or transformation was not complete yet at lower hydrothermal temperature, while the overall structure of the Cu$_{2-x}$Se-Al-140 catalyst remained largely
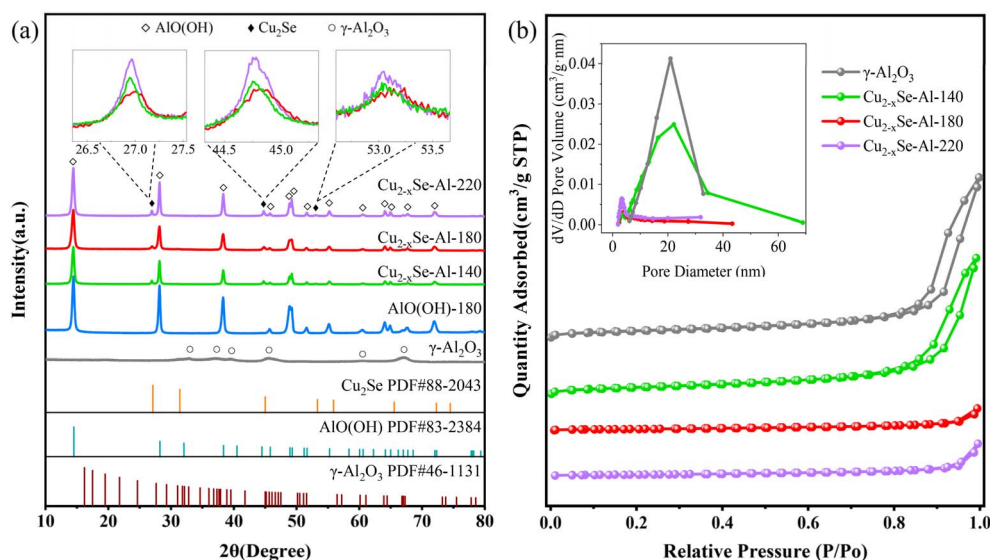

Fig. 3 (a) X-ray diffraction patterns of γ-Al$_2$O$_3$, AlO(OH)-180, Cu$_{2-x}$Se-Al-140, Cu$_{2-x}$Se-Al-180, and Cu$_{2-x}$Se-Al-220 and (b) N$_2$ adsorption–desorption isotherms.

8448 | J. Mater. Chem. A, 2025, 13, 8445–8455

This journal is © The Royal Society of Chemistry 2025

unchanged.[37] In contrast, at a hydrothermal temperature of 220 °C, the specific surface area, pore volume, and pore diameter of the catalyst were significantly reduced, from 134.5 m^2 g^{-1} to 33.1 m^2 g^{-1}, from 0.90 cm^3 g^{-1} to 0.19 cm^3 g^{-1}, and from 26.88 nm to 22.37 nm, respectively. These results suggest that temperature plays a crucial role in regulating the structure morphology of AlO(OH). Among the three distinct hydrothermal temperatures, catalyst fabricated at 180 °C exhibited the lowest specific surface area, pore volume, and pore diameter, measuring 32.53 m^2 g^{-1}, 0.13 cm^3 g^{-1}, and 15.68 nm respectively.

The hydrothermal approach is important in material preparation.[38] Intriguingly, by adjusting the hydrothermal reaction conditions, different product morphologies, crystal morphologies, and particle sizes can be obtained.[39,40] In this study, three catalysts, namely Cu$_{2-x}$Se-Al-140, Cu$_{2-x}$Se-Al-180 and Cu$_{2-x}$Se-Al-220, were analyzed using SEM and TEM techniques, with the results as shown in Fig. 4.

Based on the SEM images, the Cu$_{2-x}$Se-Al-140 catalyst hydrothermally synthesized at 140 °C (Fig. 4a) exhibits an irregular and granular structure. In contrast, the Cu$_{2-x}$Se-Al-180 catalyst synthesized at 180 °C (Fig. 4b) exhibits a sheet structure with excellent crystallinity and uniform dispersion. The Cu$_{2-x}$Se-Al-220 catalyst synthesized at a higher hydrothermal

temperature of 220 °C (Fig. 4c) retains the sheet structure, but notable aggregation is observed. This suggests that an optimal hydrothermal temperature contributes to the formation of a superior morphology, providing more active sites for the reaction.[41,42] Additionally, HAADF-STEM characterization of the three synthesized materials reveals distinct differences. The Cu$_{2-x}$Se-Al-180 catalyst fabricated at 180 °C (Fig. 4e) possesses a uniform nanosheet structure, which is distinguishes it from the Cu$_{2-x}$Se-Al-140 catalyst produced at 140 °C (Fig. 4d) and the Cu$_{2-x}$Se-Al-220 catalyst synthesized at 220 °C (Fig. 4f). XRD analysis confirms that the main phase composition of the catalyst is AlO(OH) and Cu$_2$Se. HAADF-STEM element mapping (Fig. 4g–i) confirms that the nanosheet is composed of AlO(OH). Notably, while Cu and Se elements in the Cu$_{2-x}$Se-Al-140 catalyst (Fig. 4g) and the Cu$_{2-x}$Se-Al-220 catalyst (Fig. 4i) exhibits aggregation, Cu and Se elements in the Cu$_{2-x}$Se-Al-180 catalyst (Fig. 4h), synthesized at a hydrothermal temperature of 180 °C, demonstrates excellent dispersion. This finding is consistent with the results of the XRD analysis.

The HRTEM images of the catalysts are shown in Fig. 4j–l. In the Cu$_{2-x}$Se-Al-140 catalyst (Fig. 4j), the 0.328 nm crystal spacing is attributed to the (111) facet of Cu$_2$Se, while the 0.186 nm spacing is related to the (051) facet of AlO(OH). For the Cu$_{2-x}$Se-Al-180 catalyst (Fig. 4k), the 0.201 nm spacing
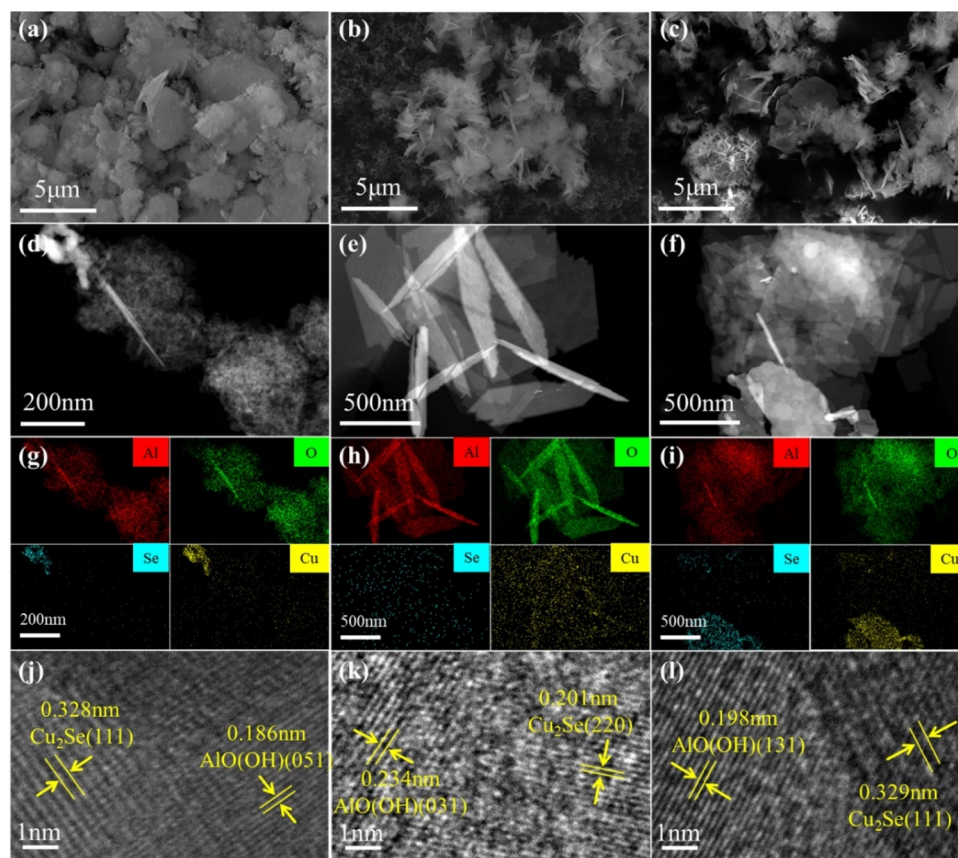

Fig. 4 From left to right, the first, second, and third columns correspond to the structural characterization maps of the three materials, Cu$_{2-x}$Se-Al-140, Cu$_{2-x}$Se-Al-180, and Cu$_{2-x}$Se-Al-220, respectively. SEM images: (a–c); HAADF-STEM images: (d–f); HAADF-STEM corresponding elemental mappings: (g–i); HRTEM images: (j–l).

corresponds to Cu_2Se (220) and the 0.234 nm spacing to AlO(OH) (031). In the $Cu_{2-x}Se$-Al-180 catalyst (Fig. 4l), the 0.329 nm crystal spacing belongs to the (111) plane of Cu_2Se, and the 0.198 nm spacing is attributed to AlO(OH) in the (131) plane. The above indicates that Cu_2Se was successfully loaded on the AlO(OH) surface in all three catalysts.[43,44]

3.3 Analysis of catalyst surface chemical properties

The catalyst was characterized using X-ray photoelectron spectroscopy (XPS) to determine the chemical valence of the material. Fig. 5 presents the XPS spectra, specifically the Cu 2p and Se 3d spectra of three catalysts, namely $Cu_{2-x}Se$-Al-140, $Cu_{2-x}Se$-Al-180, and $Cu_{2-x}Se$-Al-220.

Analysis of Fig. 5a demonstrates that the three catalysts, namely $Cu_{2-x}Se$-Al-140, $Cu_{2-x}Se$-Al-180, and $Cu_{2-x}Se$-Al-220, contain elements such as Cu, Se and O. Further analysis of the Cu 2p spectrum (Fig. 5b) reveals that the peaks adjacent to the binding energy of 933.4 eV and 953.2 eV correspond to the Cu $2p_{3/2}$ and Cu $2p_{1/2}$ orbits, respectively, suggesting the presence of Cu^{2+}. The two peaks at 940–945 eV belong to the satellite peaks of Cu^{2+} and also prove the presence of Cu^{2+} in the material. The peaks near 932.3 eV and 952.1 eV represent characteristic peaks of Cu^+ in the Cu $2p_{3/2}$ and Cu $2p_{1/2}$ orbits.[45,46] Analysis results indicate variations in the contents of Cu^{2+} and Cu^+ among the three catalysts, namely $Cu_{2-x}Se$-Al-140, $Cu_{2-x}Se$-Al-180, and $Cu_{2-x}Se$-Al-220. Particularly, the Cu^+ content of the $Cu_{2-x}Se$-Al-180 catalyst (52.29%) was significantly higher than that of the $Cu_{2-x}Se$-Al-140 catalyst (28.05%) and the $Cu_{2-x}Se$-Al-220 catalyst (38.78%). In Fig. 5c, the observed double peaks of the Se 3d orbital near 53.8 eV and 54.6 eV correspond to the Se^{2-} valence state. This suggests that the Se element exists in the form of Se^{2-} in the materials prepared under three hydrothermal conditions.[47] The $Cu_{2-x}Se$-Al-180 catalyst contains a higher amount of Cu_2Se.

Previous research has indicated that the presence of moderate basic sites enhances the adsorption and transformation of CO_2.[48] It has been observed that AlO(OH) can provide a greater number of basic sites for this process.[49] To investigate the variation in basic sites among catalysts synthesized at different hydrothermal temperatures, CO_2-TPD tests were conducted on three catalysts, namely $Cu_{2-x}Se$-Al-140, $Cu_{2-x}Se$-Al-180, and $Cu_{2-x}Se$-Al-220. The results depicted in Fig. 5d demonstrate that the basic sites of the catalyst fall into two categories: weak basic sites in the temperature range of
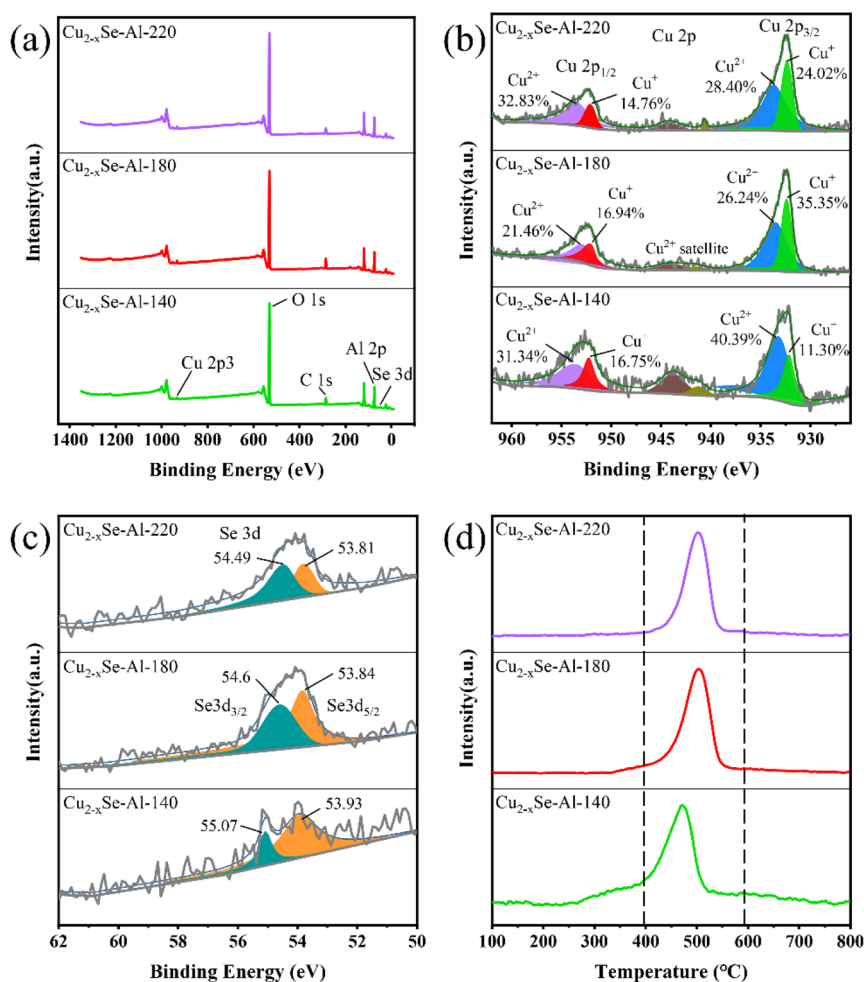

Fig. 5 (a) XPS spectra, (b) Cu 2p spectrum, (c) Se 3d spectrum, and (d) CO_2-TPD curve.

250–400 °C and moderate basic sites within the range of 400–600 °C.[50] It is evident that $Cu_{2-x}Se$-Al-140 contains both weak and moderate basic sites. At hydrothermal temperatures exceeding 180 °C, both $Cu_{2-x}Se$-Al-180 and $Cu_{2-x}Se$-Al-220 exhibit a significant presence of moderate basic sites. These findings indicate that both $Cu_{2-x}Se$-Al-180 and $Cu_{2-x}Se$-Al-220 catalysts demonstrate effective CO_2 adsorption capabilities. In addition, relevant literature indicates that Cu_2Se also has good CO_2 adsorption capacity.[51] Therefore, the $Cu_{2-x}Se$-Al-180 catalyst can provide multiple adsorption activation sites for the reaction.

Combining the above characterization results, the hydrothermal temperature was found to be the primary factor affecting the physicochemical properties of the catalysts. Specifically, the $Cu_{2-x}Se$-Al-180 and $Cu_{2-x}Se$-Al-220 catalysts have much smaller specific surface area, pore volume, and pore diameter than $Cu_{2-x}Se$-Al-140. However, they have more moderate basic sites, resulting in better CO_2 adsorption capacity. Additionally, the $Cu_{2-x}Se$-Al-180 catalysts demonstrate well-crystallized lamellar AlO(OH), better dispersed Cu_2Se, and a higher proportion of Cu^+, all of which contribute to the outstanding catalytic performance of $Cu_{2-x}Se$-Al-180.

3.4 Analysis of reaction mechanism

The XPS analysis was conducted on the $Cu_{2-x}Se$-Al-180 catalyst both before and after the reaction, in particular after a ~50 h stability test at a SIE of 58.07 kJ L^{-1}. The results depicted in Fig. 6a indicate a notable decrease in the Cu^+ ratio of the $Cu_{2-x}Se$-Al-180 catalyst from 52.29% before the reaction to 19.42% after the reaction. Conversely, the Cu^{2+} ratio exhibited an increase from 47.7% to 80.58% over the same period. These findings suggest that Cu^+ undergoes oxidation throughout the course of the reaction process.[45]

Regarding the Se element (Fig. 6b), only the presence of Se^{2-} was identified prior to the reaction. However, following the reaction, a distinct new binding energy peak emerged at 59.1 eV, corresponding to the characteristic peak of single-tooth Se^{4+}.[52] These observations provide evidence that the active component Cu_2Se in the $Cu_{2-x}Se$-Al-180 catalyst underwent transformation during the reaction.

The XRD analysis of the $Cu_{2-x}Se$-Al-180 catalyst after the reaction was compared to that before the reaction, as depicted in Fig. 6c. It was observed that the characteristic peak of AlO(OH) in the catalyst remained relatively stable after the reaction, suggesting the resilience of AlO(OH) under the DBD plasma reaction conditions. However, the diffraction peak of Cu_2Se showed a significant attenuation after the reaction. Due to the small amount of $CuSeO_3$, it was not detected in XRD, as determined by XPS characterization involved the transformation of Cu^+ into Cu^{2+} and Se^{2-} into Se^{4+}. These results indicate that the active component Cu_2Se in the $Cu_{2-x}Se$-Al-180 catalyst was converted into $CuSeO_3$ during the reaction.

Additionally, as illustrated in Fig. 7, the excited states of individual plasma, plasma-bound AlO(OH)-180, and plasma-bound $Cu_{2-x}Se$-Al-180 in the catalytic decomposition reaction of CO_2 were detected using a plasma emission spectrometer. These measurements were conducted to gain further insight into the microscopic processes underlying the reaction.
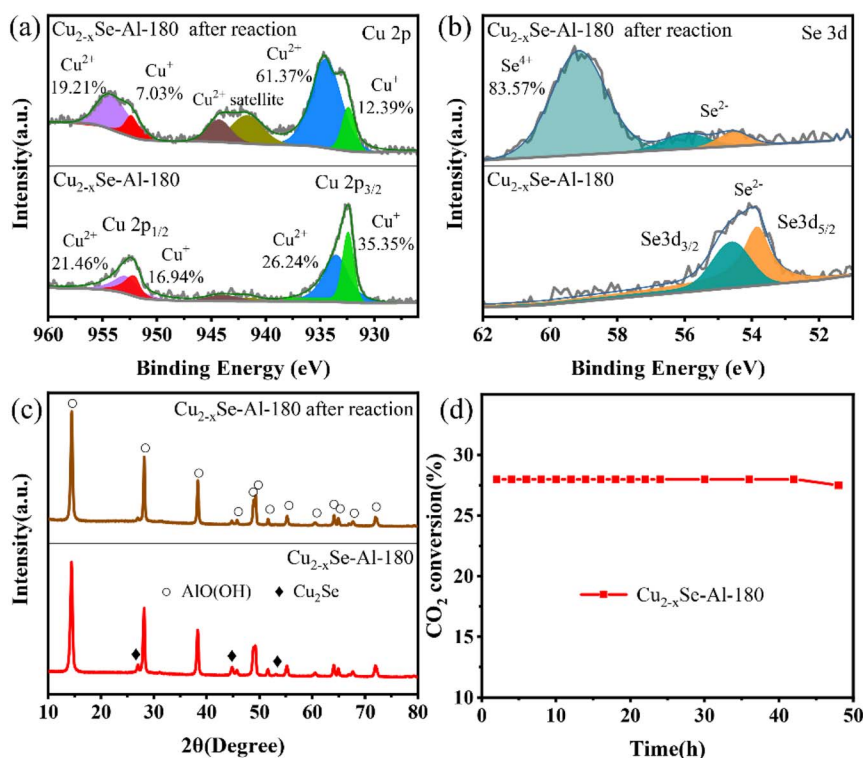

Fig. 6 (a) Cu 2p and (b) Se 3d spectra before and after the reaction of $Cu_{2-x}Se$-Al-180 catalyst. (c) Plasma emission spectra of different reaction systems; (d) stability test diagram of $Cu_{2-x}Se$-Al-180 catalyst at a SIE of 58.07 kJ L^{-1}.

This journal is © The Royal Society of Chemistry 2025
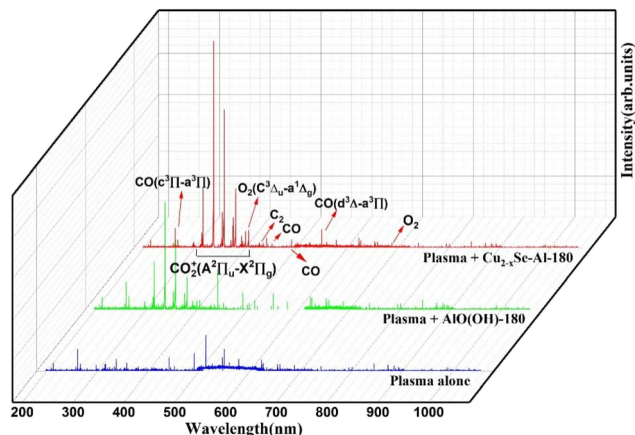
J. Mater. Chem. A, 2025, 13, 8445–8455 | 8451
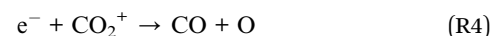
Fig. 7 Emission spectra of the reaction process.

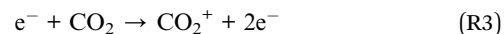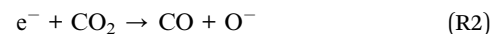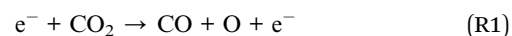The peaks within the 300–420 nm range were found to correspond to the excitation characteristic peaks of $CO_2^+(A^2\Pi_u-X^2\Pi_g)$.[53] The emission spectral peak of $CO_2^+(A^2\Pi_u-X^2\Pi_g)$ was detected across all three discharge systems within this range. However, the signal intensity of the distinctive peak was low when CO_2 was converted by a single plasma, suggesting limited excitation of CO_2 by a single plasma source. In contrast, the incorporation of AlO(OH)-180 and $Cu_{2-x}Se$-Al-180 in DBD plasma led to an enhancement in the intensity of the excitation characteristic peak of $CO_2^+(A^2\Pi_u-X^2\Pi_g)$. This enhancement indicated that the catalysts facilitated the generation of more excited species from CO_2. The characteristic peaks at approximately 210 nm, 440 nm, 490 nm, and 540 nm corresponds to $CO(d^3\Delta-a^3\Pi)$, while the characteristic peak at approximately 260 nm corresponds to CO.[54] These outcomes indicated that the conversion of CO_2 to CO was the primary reaction taking place during the process. The characteristic peaks located around 420 nm and 440 nm correspond to $C_2(A^3\Pi_g-X^3\Pi_u)$, but their intensity is extremely low, and no formation of multi-carbon products is detected. The distinct peaks observed at

approximately 390 nm and 690 nm are attributed to the $O_2(C^3\Delta_u-a^1\Delta_g)$ transition states.[55] These findings suggest that certain O excited states participate in the reaction mechanism to produce O_2. Overall, the integration of DBD plasma with the $Cu_{2-x}Se$-Al-180 catalyst enhances the activation and decomposition of CO_2.

In order to deeply investigate the reaction mechanism, *in situ* DRIFTS characterization was carried out on the $Cu_{2-x}Se$-Al-180 catalyst as shown in Fig. 8. The large peaks at 2200–2400 cm^{-1} belong to the CO_2 adsorption peaks. The peaks at 2174 cm^{-1} and 2119 cm^{-1} belong to the gaseous and weakly adsorbed CO, and the peak at 2076 cm^{-1} belongs to the bridge adsorption on the CO on $Cu_{2-x}Se$.[56,57]

The peak of CO_2 gradually weakened while the peak of CO gradually enhanced as the reaction proceeded. This suggests that CO_2 is directly converted to CO after adsorption over $Cu_{2-x}Se$-Al-180 catalyst. Previous studies have shown that the introduction of a catalyst in a plasma environment can promote CO_2 adsorption, lower the reaction activation energy barrier, and enhance the excited activation of CO_2.[58,59]

The reactions involved in this study are as in equations (R1)–(R6).[60,61] The incorporation of $Cu_{2-x}Se$-Al-180 catalyst mainly facilitated (R1)–(R3). During the reaction, accompanied by the production of (R6).

$$e^- + CO_2 \rightarrow CO + O + e^- \tag{R1}$$

$$e^- + CO_2 \rightarrow CO + O^- \tag{R2}$$

$$e^- + CO_2 \rightarrow CO_2^+ + 2e^- \tag{R3}$$

$$e^- + CO_2^+ \rightarrow CO + O \tag{R4}$$

$$O_2^- + CO_2^+ \rightarrow CO + O \tag{R5}$$

$$Cu^+ + Se^{2-} + O^- - 6e^- \rightarrow Cu^{2+} + Se^{4+} + O^{2-} \tag{R6}$$
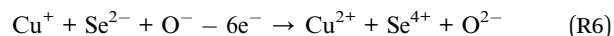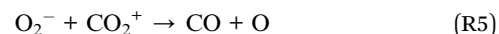
The reaction mechanism of CO_2 decomposition by the $Cu_{2-x}Se$-Al-180 catalyst in DBD plasma for CO production is

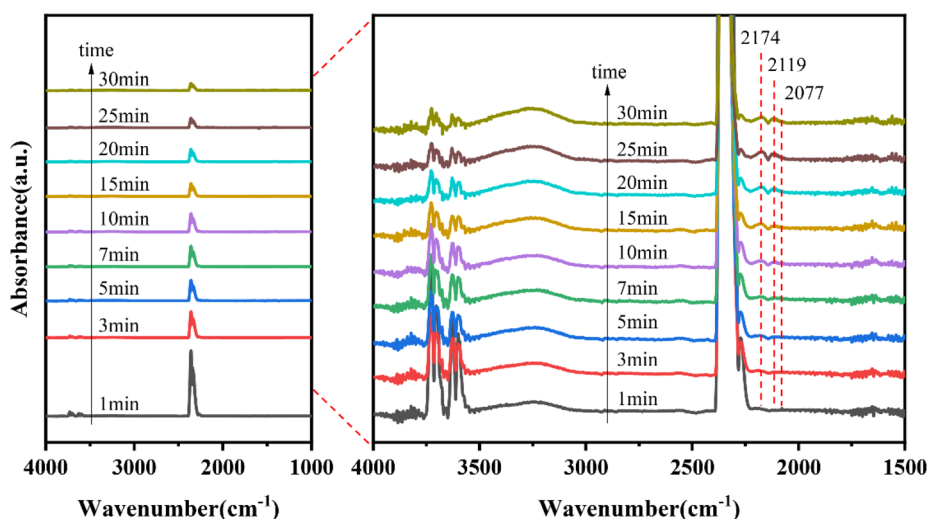

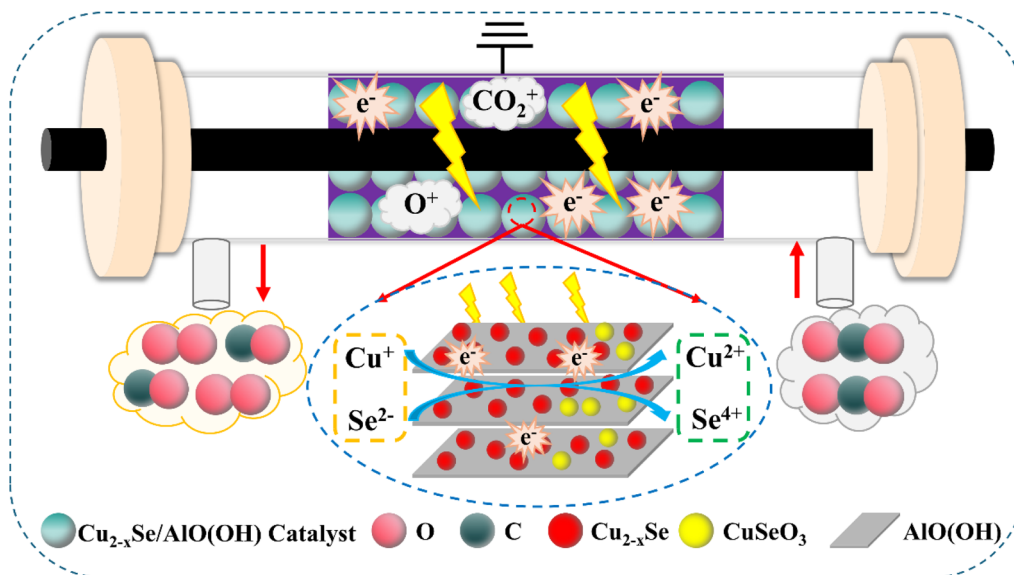Fig. 8 *In situ* DRIFTS spectra of $Cu_{2-x}Se$-Al-180 catalysts.

Fig. 9 Schematic of CO_2 decomposition by DBD plasma combined with $Cu_{2-x}Se$-Al-180 catalyst.

illustrated in Fig. 9. Overall, the incorporation of the $Cu_{2-x}Se$-Al-180 catalyst into the plasma electric field enhances the excitation and conversion of CO_2. In addition, the presence of O excited states in the electric field makes the transition from Cu_2Se to $CuSeO_3$, but this transition is slow, which is the reason why the $Cu_{2-x}Se$-Al-180 catalyst is not deactivated after a long–time reaction.

4. Conclusions

In summary, the morphology of AlO(OH), the dispersion of Cu_2Se, and the ratio of Cu^+ to Cu^{2+} during the preparation of materials *via* using the hydrothermal method were found to be influenced primarily by the hydrothermal temperature. Specifically, the $Cu_{2-x}Se$-Al-180 catalysts were prepared under hydrothermal conditions at 180 °C, resulting in the formation of nanoflake-like AlO(OH), highly dispersed Cu_2Se, and a higher Cu^+ content. The combination of $Cu_{2-x}Se$-Al-180 with DBD plasma was employed for CO_2 decomposition to generate CO, with a CO_2 conversion efficiency of up to 28.07% achieved at an SIE of 58.07 kJ L^{-1}. This remarkable effect can be attributed to the superior CO_2 adsorption properties of AlO(OH) and Cu_2Se, which lowers the activation energy barrier of the reaction and facilitates the excitation of CO_2 within the electric field of the DBD plasma, which is further enhanced by Cu_2Se. XPS and XRD characterization results indicated that the active component, Cu_2Se undergoes a transformation to $CuSeO_3$ during the reaction process, which also contributes to the gradual decline in catalyst activity.

Data availability

The data that support the findings of this study are available from the corresponding author upon reasonable request.

Author contributions

Yi Chen: investigation, writing – review & editing, writing – original draft. Weilin Shi: investigation, data curation, writing – review & editing. Claudia Li: writing – review & editing. Kang Hui Lim: data curation, writing – review & editing. Xueqian Wang: methodology, funding acquisition. Langlang Wang: methodology. Ping Ning: supervision, funding acquisition. Yixing Ma: writing – review & editing, methodology, funding acquisition, conceptualization. Sibudjing Kawi: resources, supervision.

Conflicts of interest

The authors declare that they have no known competing financial interests or personal relationships that could have appeared to influence the work reported in this paper.

References

1 L. Atwoli, A. H. Baqui, T. Benfield, R. Bosurgi, F. Godlee, S. Hancocks, R. Horton, L. Laybourn-Langton, M. C. Augusto, I. Norman, K. Patrick, N. Praities, R. M. Olde, E. J. Rubin, P. Sahni, R. Smith, N. Talley, S. Turale and D. Vazquez, *Global Health Action*, 2021, **14**, 1965745.

2 F. Bakhtiari, *Clim. Policy*, 2018, **18**, 655–663.

This journal is © The Royal Society of Chemistry 2025

J. Mater. Chem. A, 2025, **13**, 8445–8455 | **8453**

3 L. Zhang, Y. Song, J. Shi, Q. Shen, D. Hu, Q. Gao, W. Chen, K. Kow, C. Pang, N. Sun and W. Wei, *Adv. Atmos. Sci.*, 2022, **39**, 1252–1270.

4 T. Nunnally, K. Gutsol, A. Rabinovich, A. Fridman, A. Gutsol and A. Kemoun, *J. Phys. D*, 2011, **44**, 274009.

5 J. Chen, J. Ma, M. B. Alford, Y. Sun, J. Tong and F. Peng, *ACS Appl. Energy Mater.*, 2021, **4**, 10451–10458.

6 J. Gao, J. Li, Y. Liu, M. Xia, Y. Z. Finfrock, S. M. Zakeeruddin, D. Ren and M. Grätzel, *Nat. Commun.*, 2022, **13**, 5898.

7 W. Lin, J. Lin, X. Zhang, L. Zhang, R. A. Borse and Y. Wang, *J. Am. Chem. Soc.*, 2023, **145**, 18141–18147.

8 Y. Han, S. An, X. Zhan, L. Hao, L. Xu, S. Hong, D. Park, Y. Chen, Y. Xu, J. Zhao, X. Tan, A. W. Robertson, Y. Jung and Z. Sun, *CCS Chem.*, 2024, **6**, 1477–1486.

9 B. Tian, H. Wu, Y. Zhang, C. Chen, K. K. Abdalla, M. G. Sendeku, L. Zhou, J. Yu, Y. Wang, Y. Kuang, H. Xu, J. Li and X. Sun, *ACS Catal.*, 2024, 10904–10912.

10 A. Zhanaidarova, S. C. Jones, E. Despagnet-Ayoub, B. R. Pimentel and C. P. Kubiak, *J. Am. Chem. Soc.*, 2019, **141**, 17270–17277.

11 D. Ray, R. Saha and S. Ch, *Catalysts*, 2017, **7**, 244.

12 R. Aerts, W. Somers and A. Bogaerts, *ChemSusChem*, 2015, **8**, 702–716.

13 S. Adabala and D. P. Dutta, *J. Environ. Chem. Eng.*, 2022, **10**, 107763.

14 J. Li, W. Zhang and W. Zheng, *Small*, 2024, 20.

15 X. Xia, L. Wang, N. Sui, V. L. Colvin and W. W. Yu, *Nanoscale*, 2020, **12**, 12249–12262.

16 K. H. Cho, J. Heo, Y. M. Sung and P. K. Jain, *Angew. Chem., Int. Ed. Engl.*, 2019, **58**, 8410–8415.

17 O. Ohsawa, M. Iwase and H. Okimura, *Jpn. J. Appl. Phys.*, 1980, **19**, 165.

18 A. Saxena, W. Liyanage, J. Masud, S. Kapila and M. Nath, *J. Mater. Chem. A*, 2021, **9**, 7150–7161.

19 A. Ali and W. Oh, *Fullerenes, Nanotubes, Carbon Nanostruct.*, 2016, **24**, 555–563.

20 A. Ali, D. Cung Tien Nguyen, K. Cho and W. Oh, *Fullerenes, Nanotubes, Carbon Nanostruct.*, 2018, **26**, 827–836.

21 B. Li, J. Xiong, C. Peng, M. Li, H. Liu, W. Wang and S. Peng, *Ceram. Int.*, 2023, **49**, 38226–38236.

22 A. E. Creamer, B. Gao and S. Wang, *Chem. Eng. J.*, 2016, **283**, 826–832.

23 Z. Chen, Z. Ma, G. Fan and F. Li, *ACS Appl. Mater. Interfaces*, 2024, **16**, 35144–35154.

24 I. Michielsen, Y. Uytdenhouwen, J. Pype, B. Michielsen, J. Mertens, F. Reniers, V. Meynen and A. Bogaerts, *Chem. Eng. J.*, 2017, **326**, 477–488.

25 D. Yap, J. Tatibouët and C. Batiot-Dupeyrat, *J. CO$_2$ Util.*, 2015, **12**, 54–61.

26 Z. Liu, W. Zhou, Y. Xie, F. Liu, Z. Fang, G. Zhang and W. Jin, *J. Membr. Sci.*, 2023, **685**, 121981.

27 N. Lu, N. Liu, C. Zhang, Y. Su, K. Shang, N. Jiang, J. Li and Y. Wu, *Chem. Eng. J.*, 2021, **417**, 129283.

28 Z. Qin, J. Ren, M. Miao, Z. Li, J. Lin and K. Xie, *Appl. Catal., B*, 2015, **164**, 18–30.

29 R. Wei, Z. Gao and W. Huang, *Mol. Catal.*, 2023, **548**, 113457.

30 L. Yixuan, L. Chenxia, D. Degang, D. Bin, W. Le and X. Shiqing, *Optik*, 2018, **154**, 171–176.

31 C. V. S. Almeida, K. I. B. Eguiluz and G. R. Salazar-Banda, *J. Electroanal. Chem.*, 2020, **878**, 114683.

32 Y. Wang, B. Wang, J. Zhang, D. Chao, J. Ni and L. Li, *Carbon Energy*, 2022, **5**, e202100459.

33 J. Y. C. Liew, Z. A. Talib, Z. Zainal, M. A. Kamarudin, N. H. Osman and H. K. Lee, *Semicond. Sci. Technol.*, 2019, **34**, 125017.

34 M. Thommes, K. Kaneko, A. V. Neimark, J. P. Olivier, F. Rodriguez-Reinoso, J. Rouquerol and K. S. W. Sing, *Pure Appl. Chem.*, 2015, **87**, 1051–1069.

35 S. O. Kazantsev, K. V. Suliz, N. G. Rodkevich and A. S. Lozhkomoev, *Materials*, 2023, **16**, 6057.

36 Z. Tang, J. Liang, X. Li, J. Li, H. Guo, Y. Liu and C. Liu, *J. Solid State Chem.*, 2013, **202**, 305–314.

37 C. Hai, L. Zhang, Y. Zhou, X. Ren, J. Liu, J. Zeng and H. Ren, *J. Inorg. Organomet. Polym. Mater.*, 2018, **28**, 643–650.

38 R. Wu, P. Xie, Y. Cheng, Y. Yue, S. Gu, W. Yang, C. Miao, W. Hua and Z. Gao, *Catal. Commun.*, 2013, **39**, 20–23.

39 H. Yin, J. Liu, H. Shi, L. Sun, X. Yuan and D. Xia, *Process Saf. Environ. Protect.*, 2022, **162**, 944–954.

40 W. Chen, Y. Wang, S. Liu, L. Gao, L. Mao, Z. Fan, W. Shangguan and Z. Jiang, *Appl. Surf. Sci.*, 2018, **445**, 527–534.

41 L. Yubiao, C. Rui, L. Yu, W. Langlang, N. Ping, W. Xueqian and M. Yixing, *Fuel*, 2024, **373**, 132390.

42 L. Tang, X. Jiang, Q. Zheng and D. Lin, *Dalton Trans.*, 2021, **51**, 211–219.

43 H. Peng, W. Miao, S. Cui, Z. Liu, X. Wang, B. Tao, W. Hou, Z. Zhang and G. Ma, *Chem. Eng. J.*, 2024, **487**, 150701.

44 W. Fu, Q. Zhan, Y. Yu, X. Meng, M. Tang, Y. Wang, Y. Sun and Y. Dai, *ChemNanoMat*, 2022, **8**, e202100459.

45 W. Sun, P. Wang, Y. Jiang, Z. Jiang, R. Long, Z. Chen, P. Song, T. Sheng, Z. Wu and Y. Xiong, *Adv. Mater.*, 2022, **34**, e2207691.

46 L. Yang, J. Wei, Y. Qin, L. Wei, P. Song, M. Zhang, F. Yang and X. Wang, *Materials*, 2021, **14**, 2075.

47 X. Hua, J. Li, H. Liu, C. Zhang, Y. Han, F. Gao, G. Hodes, P. Wang, Z. Yang and S. F. Liu, *Vacuum*, 2021, **185**, 109947.

48 V. Meeyoo, N. Panchan, N. Phongprueksathat, A. Traitangwong, X. Guo, C. Li and T. Rirksomboon, *Catalysts*, 2020, **10**, 32.

49 M. Ma, H. Liu, J. Cao, P. Hou, J. Huang, X. Xu, H. Yue, G. Tian and S. Feng, *Mol. Catal.*, 2019, **467**, 52–60.

50 E. Choi, K. Song, S. An, K. Lee, M. Youn, K. Park, S. Jeong and H. Kim, *Korean J. Chem. Eng.*, 2018, **35**, 73–81.

51 L. Ding, N. Zhu, Y. Hu, Z. Chen, P. Song, T. Sheng, Z. Wu and Y. Xiong, *Angew. Chem., Int. Ed.*, 2022, **61**, e202209268.

52 S. C. Riha, D. C. Johnson and A. L. Prieto, *J. Am. Chem. Soc.*, 2011, **133**, 1383–1390.

53 H. Wang, Y. Yang, Z. Li, X. Kong, P. Martin, G. Cui and R. Wang, *Int. J. Hydrogen Energy*, 2023, **48**, 8921–8931.

54 F. Ahmad, E. C. Lovell, H. Masood, P. J. Cullen, K. K. Ostrikov, J. A. Scott and R. Amal, *ACS Sustainable Chem. Eng.*, 2020, **8**, 1888–1898.

8454 | *J. Mater. Chem. A*, 2025, **13**, 8445–8455

This journal is © The Royal Society of Chemistry 2025

55 D. Mei, X. Shen, S. Liu, R. Zhou, X. Yuan, Z. Rao, Y. Sun, Z. Fang, X. Du, Y. Zhou and X. Tu, *Chem. Eng. J.*, 2023, **462**, 142044.

56 H. Zuo, C. Lu, L. Jiang, X. Cheng, Z. Li, Y. Li, D. Li, H. Wang and K. Li, *Chem. Eng. J.*, 2023, **477**, 146870.

57 B. Liu, Y. Sun, M. Li, Z. Fan, X. Chen, X. Lan, Q. Zhong and T. Wang, *ACS Catal.*, 2024, **14**, 15956–15964.

58 N. Lu, X. Jiang, Y. Zhu, L. Yu, S. Du, J. Huang and Z. Zhang, *Adv. Mater.*, 2024, **37**, e2413931.

59 G. Wang, S. Zhong, X. Xiong, J. Li, F. Wang, L. Huo, D. Wu, X. Han, Z. Wang, Q. Chen, X. Tian and P. Deng, *J. Energy Chem.*, 2024, **95**, 636–643.

60 R. Hosseini Rad, V. Brüser, M. Schiorlin, J. Schäfer and R. Brandenburg, *Chem. Eng. J.*, 2023, **456**, 141072.

61 M. Umamaheswara Rao, K. Bhargavi, G. Madras and C. Subrahmanyam, *Chem. Eng. J.*, 2023, **468**, 143671.

This journal is © The Royal Society of Chemistry 2025

J. Mater. Chem. A, 2025, **13**, 8445–8455 | **8455**